ACS APPLIED MATERIALS & INTERFACES

Research Article

www.acsami.org

Polyaniline-Decorated {001} Facets of $Bi_2O_2CO_3$ Nanosheets: In Situ Oxygen Vacancy Formation and Enhanced Visible Light Photocatalytic Activity

Ziyan Zhao,[†,‡] Ying Zhou,[*,†,‡] Fang Wang,[‡] Kunhao Zhang,[§] Shan Yu,[‡] and Kun Cao[‡]

[†]State Key Laboratory of Oil and Gas Reservoir and Exploitation and [‡]School of Materials Science and Engineering, Southwest Petroleum University, Chengdu 610500, China

[§]Shanghai Synchrotron Radiation Facility, Shanghai Institute of Applied Physics, Chinese Academy of Sciences, Shanghai 201204, China

Supporting Information

ABSTRACT: Polyaniline (PANI)-decorated {001} facets of $Bi_2O_2CO_3$ nanosheets were synthesized by a low-temperature chemical method. We demonstrate that the strong interfacial interactions between $Bi_2O_2CO_3$ {001} facets and PANI could promote in situ formation of oxygen vacancy at the interface confirmed by both density functional theory calculations and electron spin resonance experiments, which is due to the high oxygen density characteristic of $Bi_2O_2CO_3$ {001} facets. In addition, such interfacial interaction also leads to a 0.38 eV positive shifting of the valence band of $Bi_2O_2CO_3$. Importantly, the decorated PANI can stabilize these interfacial oxygen vacancies. Therefore, the migration and separation of photogenerated carriers have been improved significantly evidenced by electrochemical impedance spectroscopy, photoluminescence, and nanosecond time-resolved fluorescence-decay spectra, resulting in a 4.5 times higher activity toward photodegradation of Rhodamine B and a 6 times higher photocurrent density compared to their corresponding bare $Bi_2O_2CO_3$. The finding of the in situ oxygen vacancy formation at the interface could provide some hints for the deep understanding of the interactions between PANI and crystal facets of semiconductors to develop highly efficient photocatalysts.

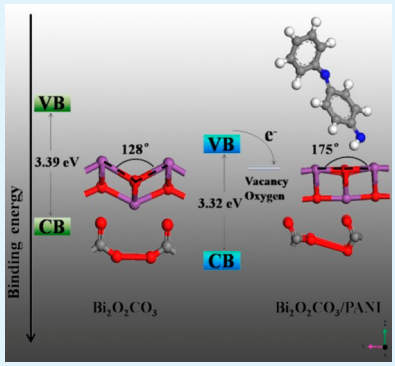

KEYWORDS: *$Bi_2O_2CO_3$/PANI, interfacial interaction, oxygen vacancy, crystal facets, photocatalysis*

1. INTRODUCTION

Semiconductor-based photocatalysis has attracted considerable attention as a potential solution for dealing with global energy crisis and environmental pollution.[1,2] Yet, until now, the overall photocatalytic efficiency is still very low and is limited by the low sunlight harvesting and the slow electron transfer and fast charge recombination, which require further promotion for photocatalytic applications. Among the investigated photocatalysts, materials with layered structure attract increasing interest due to their anisotropic crystal structure and internal static electric field effect, which favors the photoinduced charge separation and transfer.[3,4] Sillén-type $Bi_2O_2CO_3$ with alternating $Bi_2O_2^{2+}$ and CO_3^{2-} layers (cf. Supporting Information, Figure S1) bears close resemblance to the Aurivillius-type oxides, and it was first applied by Zheng et al. as a photocatalyst for the degradation of Rhodamine B (RhB) in aqueous solution.[5] This was followed by the development of various synthetic routes to nanostructured $Bi_2O_2CO_3$ photocatalysts[6−9] as illustrated by some selected examples: sponge-, rose-, and plate-shaped $Bi_2O_2CO_3$ were hydrothermally prepared by Zhao et al.,[10] and its combination with polyacrylamide as morphology mediator led to persimmon-like $Bi_2O_2CO_3$ particles.[11] Furthermore, coupling $Bi_2O_2CO_3$ with other semiconductors including C_3N_4,[12] Ag_2O,[13] Bi_2WO_6,[14] Bi_2MoO_6,[15] Bi_2O_3,[16] and BiOI[17] has been clearly demonstrated to improve their photocatalytic activities. In particular, the $Bi_2O_2CO_3$ {001} facets possess a higher oxygen atom density than {010} and {110} counterparts (Supporting Information, Figure S1), which not only contribute to the high efficiency of photocatalysts[5] but also provide a noteworthy model material to investigate the interfacial interaction between $Bi_2O_2CO_3$ and other materials.

On the other hand, the conducting polymers with extending π-conjugated electron systems, such as polyaniline (PANI), polypyrrole (PPy), and polythiophene (PT), have shown great potential applications due to their high absorption coefficient in the visible-light range, high mobility of charge carriers, and excellent stability.[18] Recently, some studies have clearly demonstrated that the combination of PANI with semiconductor photocatalysts including TiO_2,[19] ZnO,[20] C_3N_4,[21] BiOCl,[22] $Bi_{12}TiO_{20}$,[23] and Bi_2WO_6[24] can improve their photocatalytic performances. Nevertheless, the photocatalytic applications of $Bi_2O_2CO_3$/PANI have never been explored to the best of our knowledge. More importantly, although the synergic effect between PANI and semiconductors, which can

Received: October 14, 2014
Accepted: December 12, 2014
Published: December 12, 2014

DOI: 10.1021/am507089x
ACS Appl. Mater. Interfaces 2015, 7, 730−737

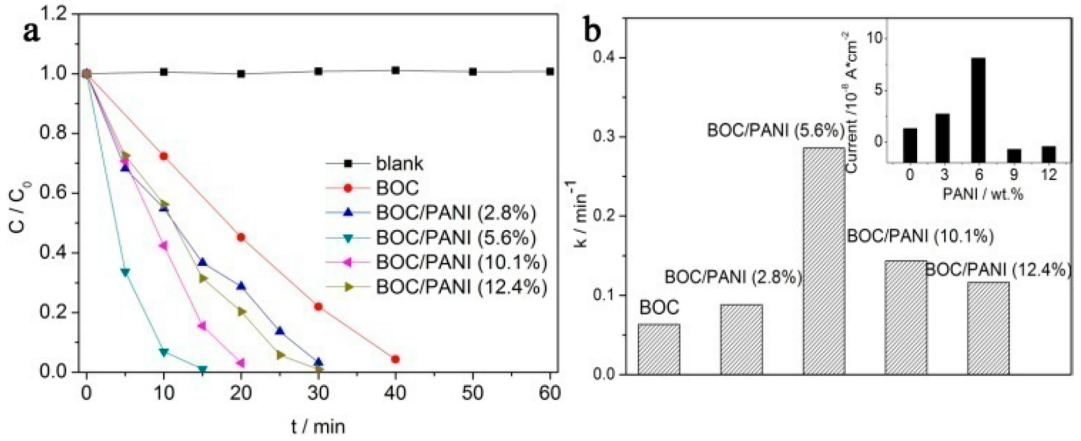

Figure 1. (a) Photodegradation of RhB over different photocatalysts under visible light irradiation (λ > 420 nm). (b) Comparison of the corresponding kinetic constants. (inset) Photocurrent of these photocatalysts.

enhance light absorption and improve separation and transfer of photogenerated carriers at their interfaces, is usually deemed responsible for the enhanced photocatalytic activity in general,[19−24] the in-depth and comprehensive understanding of the interfacial interactions between PANI and semiconductors has seldom been explored, especially on the basis of certain crystal facets of semiconductors.[25−27]

Herein, we synthesized PANI-decorated {001} facets of $Bi_2O_2CO_3$ nanosheets through a facile low-temperature chemical approach. The $Bi_2O_2CO_3$ {001} facets with high density of oxygen atoms not only lead to intimate contact between PANI and $Bi_2O_2CO_3$ but also promote in situ formation of oxygen vacancies at the interface during coupling with PANI process evidenced by both experiments and theoretical calculations. The strong interfacial interactions between PANI and $Bi_2O_2CO_3$ {001} facets have significant influence on their band structures as well as charge separation and migration processes, which finally resulted in a notably enhanced visible light driven photocatalytic activity. The finding of the in situ oxygen vacancy formation at the interface undoubtedly provides a new strategy to develop photocatalysts with high activity.

2. EXPERIMENTAL SECTION

2.1. Synthesis of $Bi_2O_2CO_3$ Nanosheets and $Bi_2O_2CO_3$/PANI Composites. PANI was synthesized according to the reported method.[19] $Bi_2O_2CO_3$ nanosheets with exposed {001} facets were prepared via a low-temperature chemical method modified from a previous work.[7] Typically, 48.5 g (0.1 mol) of $Bi(NO_3)_3{\cdot}5H_2O$ was first dissolved in 100 mL of 1 M HNO_3 (denoted as solution A). Meanwhile, 84.5 g (0.8 mol) of Na_2CO_3 and 10 g of cetyltrimethylammonium bromide (CTAB) were added into 900 mL of distilled water (denoted as solution B). Then, solution B was added into solution A under stirring at 30 °C for 30 min. After that the final products were washed several times with isopropyl alcohol and distilled water and dried at 60 °C for 12 h. The $Bi_2O_2CO_3$/PANI composites were prepared as follows: 400 mg of the obtained $Bi_2O_2CO_3$ was added into 0.45 g/L PANI/tetrahydrofura (THF) solution with different volume (25, 50, 90, and 110 mL), subjected to ultrasound for 1 h, and then stirred for 24 h at room temperature. Finally, the suspension was centrifuged and washed by distilled water and ethanol and dried at 60 °C for 12 h.

2.2. Characterization. Powder X-ray diffraction (PXRD) was recorded on a PANalytical X'pert diffractometer operated at 40 kV and 40 mA using Cu Kα radiation. The morphology of the prepared samples was examined using a scanning electron microscopy (SEM) (Hitachi S-4800). Transmission electron microscopy (TEM) and high-resolution TEM (HRTEM) images were obtained on FEI Tecnai G2 20 microscopy operated at 200 kV. The Fourier transform infrared (FT-IR) spectra were performed on a Nicolet 6700 spectrometer on samples embedded in KBr pellets. X-ray photoelectron spectroscopy (XPS) measurements were investigated on a Thermo ESCALAB 250Xi with Al Kα emission at 1486.6 eV, and all of the binding energies were referenced to the C 1s at 284.8 eV. UV−vis spectra were performed on a Shimadzu 2600 UV−vis spectrophotometer. A JES FA200 spectrometer was used to detect the electron spin resonance (ESR) signals of the samples at room temperature. Steady-state and transient fluorescence spectra were both measured using FLSP-920 (Edinburgh Instruments). A Xe light was used as the light source for steady-state spectra with excitation wavelength of 375 nm, while a 375 wavelength pulse laser (pulse width 70 ps) was used for transient spectra. The detection wavelength for time-resolved emission decay is 440 nm.

2.3. Density Functional Theory Calculations. The first-principle calculations were performed by the CASTEP package[28] with the Vanderbilt-type ultrasoft pseudopotential and a plane-wave expansion of the wave functions. The generalized gradient approximation (GGA) of Perdew−Burke−Ernzerh (PBE) was applied to account for the exchange correlation function. The cutoff energy was set to 380 eV, and the self-consistent field interaction was 2.0×10^{-6} eV. Brillouin zone intergrations were approximated by using the Monkhorst−Pack grid of 1 × 2 × 1 k-points. The BOC (001) slab was separated by a vacuum spacing of 20 Å to avoid the interactions between periodic images. A 2 × 1 (001) slab composed of four atomic layers was used with two bottom layers fixed at the bulk position.

2.4. Photoelectrochemical and Photocatalytic Activity Tests. Photoelectrochemical (PEC) measurements were conducted in a conventional three-electrode system with 0.5 M Na_2SO_4 electrolyte on a CHI 660 electrochemical workstation. The obtained samples were deposited on fluorine-doped tin oxide (FTO) conducting glass electrodes as the working electrodes, while the saturated calomel electrode (SCE) and platinum wire were the reference electrode and the counter electrodes, respectively. The photocurrent−time dependent experiments at open circuit potential (OCV) were under chopped illumination with a MVL-210 (Mejiro Genossen Inc.) visible light source (λ > 378 nm). The photocatalytic activity of these samples was evaluated by the photodegradation of RhB under visible light irradiation using 300 W Xe lamp (λ > 420 nm) as the light source. Prior to illumination, 100 mg of the photocatalyst powders were suspended in 150 mL of RhB solution (3×10^{-5} mol/L) and stirred for 60 min to reach an adsorption−desorption equilibrium. The initial pH value of RhB solution is 4.4. Aliquots (2.5 mL) of suspension were taken after selected time intervals. Residual catalyst was removed by centrifugation (10 000 r/min for 10 min), and the concentration of RhB was monitored on a UV-5100 (Anhui Wanyi) spectrophotometer. Photocatalytic oxidation of NO was measured at ppb levels in a

DOI: 10.1021/am507089x
ACS Appl. Mater. Interfaces 2015, 7, 730−737

continuous flow reactor at the ambient temperature. Details of the reactor setup can be referred to our previous work.[29]

3. RESULTS AND DISCUSSION

3.1. Photocatalytic Activity and Photocurrent Test. PANI hybridized $Bi_2O_2CO_3$ (BOC) samples with different mass ratios from 2.8 to 12.4% were prepared, which are denoted BOC/PANI (2.8%), BOC/PANI (5.6%), BOC/PANI (10.1%), and BOC/PANI (12.4%). Photocatalytic activity of the prepared samples was evaluated by photodegradation of RhB in aqueous solution under visible light irradiation ($\lambda > 420$ nm), which is a commonly used method to evaluate the activity of photocatalysts.[30,31] Figure 1a displays the temporal evolution of RhB concentration in the presence of the prepared samples. The photolysis of RhB in the absences of photocatalysts is negligible within the test period. As expected, all of the $Bi_2O_2CO_3$/PANI composites exhibited higher activities than the pristine $Bi_2O_2CO_3$. Furthermore, the photocatalytic activities of $Bi_2O_2CO_3$/PANI samples are a function of the mass ratios between PANI and BOC. The photocatalytic performance of BOC/PANI (5.6%) exceeded all other samples by far: the main absorption of RhB at 554 nm disappeared almost entirely after only 15 min of visible light irradiation. The corresponding rate constant k was calculated to be ~0.286 min^{-1} (as shown in Figure 1b), which is ~4.5 times faster than that of BOC (0.063 min^{-1}). Supporting Information, Figure S2 shows the adsorption of RhB over BOC and BOC/PANI with different mass ratios in the dark. All of the BOC/PANI samples exhibited higher adsorption of RhB in the dark compared to the pure BOC. The BET surface area of BOC and BOC/PANI (5.6%) was determined as 14.3 and 17.4 m^2/g, respectively. After normalizing the k to the specific surface area, BOC/PANI (5.6%) still exhibited ~4 times higher activity than that of BOC (Supporting Information, Figure S3), indicating that the enhanced photocatalytic activities were not ascribed to the surface area. In addition, the photocatalytic activities of BOC and BOC/PANI (5.6%) were further evaluated for the photooxidation of NO at the indoor air level. Under visible light irradiation, the photodegradation of NO over BOC is quite low, whereas the removal ratio of NO over BOC/PANI (5.6%) can reach as high as 54% within 5 min (Supporting Information, Figure S4). All of these results clearly confirm that the photocatalytic activity of BOC can be significantly enhanced through coupling with PANI. The reusability of BOC/PANI (5.6%) was evaluated based on the recycling experiments. After the first run, the activity of BOC/PANI (5.6%) decreased slightly due to surface contamination, and then it kept stable (Supporting Information, Figure S5). In addition, the activity of BOC/PANI (5.6%) can be as high as the fresh sample even after exposing in air for four months (Supporting Information, Figure S6). Moreover, it is worth noting that the photocurrent tests of these samples displayed the same trend as the degradation performance (inset, Figure 1b). The photocurrent of BOC/PANI (5.6%) is 8.1×10^{-8} A/cm^2, which is 6 times higher than that of BOC (1.3×10^{-8} A/cm^2). Therefore, BOC/PANI (5.6%) is recommended to be the optimal composite among the series prepared samples on the basis of photodegradation and photocurrent measurements.

3.2. Morphology and Microstructures. Supporting Information, Figure S7 shows the PXRD patterns of the pristine BOC and BOC/PANI (5.6%) composite. The observed peaks of BOC can be well-indexed to tetragonal $Bi_2O_2CO_3$ (JCPDS card No. 41−1448). Notably, the diffraction ratio (0.85) of (110)/(013) planes for BOC is much higher than the standard value (0.38), indicating a bias of orientations long {110} crystallographic plane.[6−9] After coupling with PANI, all of the diffraction peaks of BOC/PANI (5.6%) are nearly identical to those of BOC. Generally, PANI exhibits a broad peak at approximately 20−25°.[20] No such characteristic peak of PANI is detected, revealing a very low loading amount of PANI and high dispersion of PANI on the surface of BOC.[18] FT-IR spectra of BOC, PANI, and BOC/PANI (5.6%) are shown in Supporting Information, Figure S8. The peaks at 1390, 1068, and 846 cm^{-1} are assigned to the CO_3^{2-} group,[32] while those at 1133 and 1566 cm^{-1} are assigned to the C−H bending in-plane bending of quinonoid units and the C═N stretching modes of vibration for quinonoid units of PANI.[33] BOC/PANI (5.6%) shows the characteristic bands of both BOC and PANI, confirming the existence of PANI in the composite.

SEM observations revealed that the BOC consisted of large scale sheet-shaped morphologies with width from 30 to 300 nm and thickness from 7 to 16 nm (Figure 2a). These two-dimensional (2D) nanosheets were formed due to the internal layered crystal structure of $Bi_2O_2CO_3$ with weak van der Waals interactions along the [001] direction (Figure S1).[6−9] After coupling with PANI, the morphology and size of BOC/PANI (5.6%) kept almost unchanged and had a smooth surface (as shown in Figure 2b). These indicated that PANI could disperse uniformly on the surface of BOC. In addition, Supporting Information, Figure S9 and S10 show the PXRD pattern and SEM image of BOC/PANI (5.6%) after cycling tests. No significant structural and morphological changes were observed.

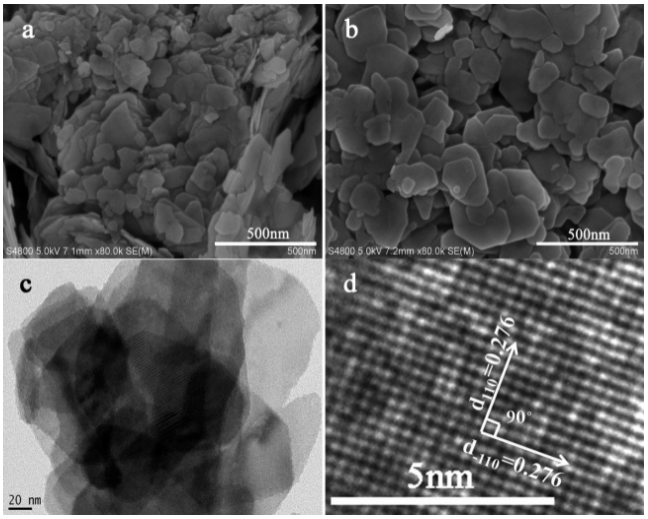

Figure 2. SEM images of (a) BOC and (b) BOC/PANI (5.6%). (c) TEM and (d) HRTEM images of BOC/PANI (5.6%).

TEM images of BOC/PANI (5.6%) further confirmed the 2D sheet-shaped morphology (Figure 2c). Especially, these nanosheets are very thin and are mostly transparent under electron beam (Figure 2c). The HRTEM image (Figure 2d) exhibits the highly crystalline nature of BOC/PANI (5.6%). The fringe spacing of 0.276 nm and an angle of 90° match well with the (110) atomic planes of tetragonal $Bi_2O_2CO_3$, which are consistent with the results from PXRD patterns (Figure S7). On the basis of these results, the wide surface of BOC/PANI (5.6%) can be unambiguously identified as {001} facets, which is characterized by the high density of oxygen atoms

DOI: 10.1021/am507089x
ACS Appl. Mater. Interfaces 2015, 7, 730−737

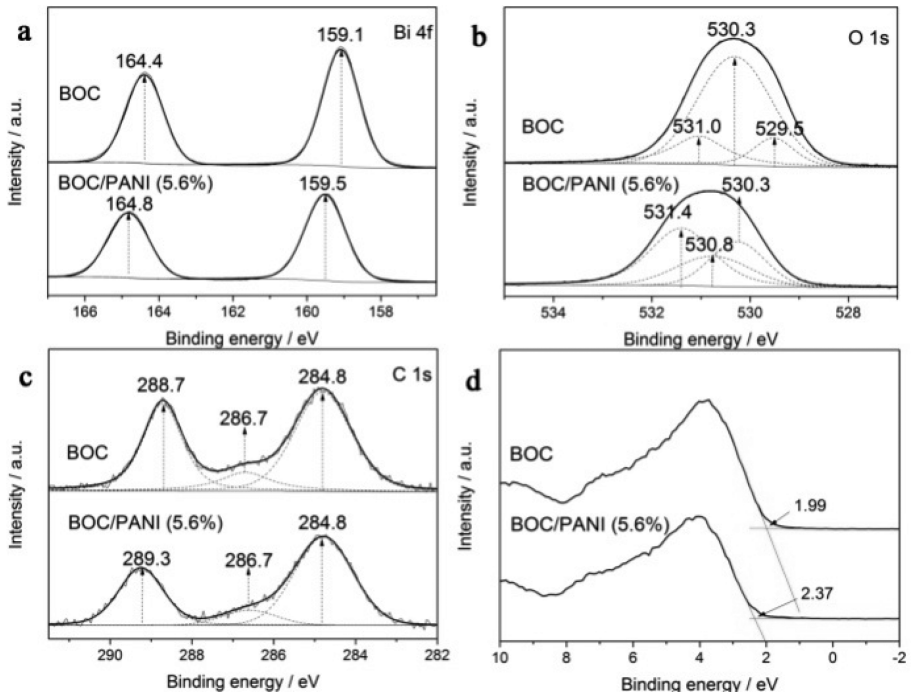

Figure 3. (a) Bi 4f, (b) O 1s, and (c) C 1s XPS spectra of BOC and BOC/PANI (5.6%); (d) valence band XPS spectra of BOC and BOC/PANI (5.6%).

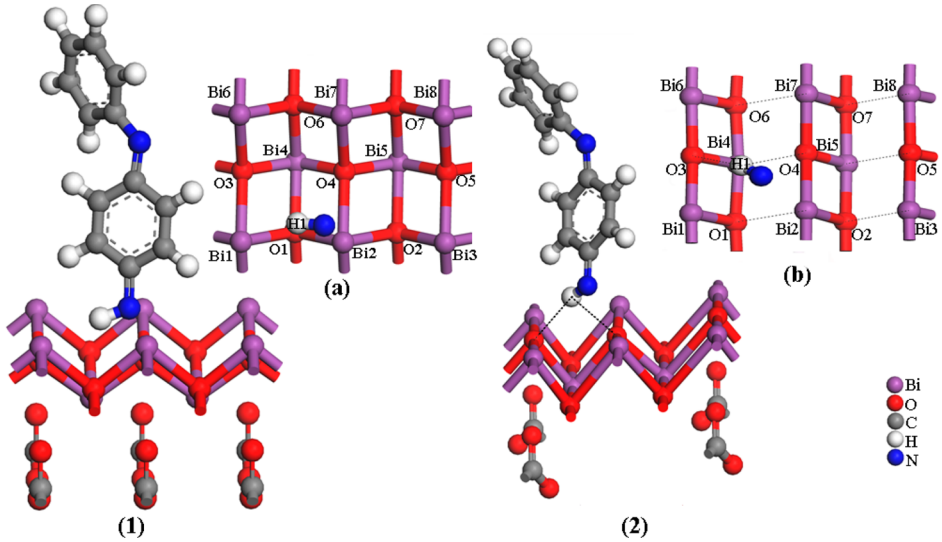

Figure 4. (1) Computational model of the PANI/$Bi_2O_2CO_3$ (001) interface and (2) optimized interface structure (a) and (b) represent the top view the PANI/$Bi_2O_2CO_3$ (001) interface for the computational and optimized geometries, respectively.

(Figure S1). These oxygen atoms exposed on the surface could provide active sites to bond with PANI. Furthermore, the HRTEM image (Supporting Information, Figure S11) of BOC/PANI (5.6%) displays a distinct PANI noncrystal edge with a thickness from 0.6−3 nm, revealing a tight contact between BOC and PANI.

3.3. The Interfacial Interactions. The interactions between BOC nanosheets and PANI are further investigated by XPS. The two characteristic peaks for Bi 4f located at 164.4 and 159.1 eV in Figure 3a are attributed to Bi $4f_{5/2}$ and Bi $4f_{7/2}$ in BOC.[34] After loading the PANI, these peaks in BOC/PANI (5.6%) were shifted up by 0.4 eV. Besides, the peaks of O 1s at 529.5, 530.3, and 531.0 eV were shifted to 530.3, 530.8, and 531.4 eV, respectively (Figure 3b). Consequently, compared to BOC, the binding energies of both O and Bi atoms in BOC/PANI (5.6%) shifted positively, indicating the presence of strong interactions between BOC and PANI, which led to alternate the distribution of the electric charge of Bi and O atoms in the composite. Figure 3c shows the C 1s spectra of BOC and BOC/PANI (5.6%). The peaks at 284.8 and 286.7 eV can be assigned to adventitious carbon species from XPS measurements,[8] which keep unchanged, while the peak at 288.7 eV ascribing to carbonate ion in BOC were shifted up to 289.3 eV after coupling with PANI. Therefore, the strong interaction between BOC and PANI could influence the electronic distribution of C in the CO_3^{2-} layers as well. Obviously, the decoration of PANI on the surface of BOC altered the charge

DOI: 10.1021/am507089x
ACS Appl. Mater. Interfaces 2015, 7, 730−737

Table 1. Length of Hydrogen Bonds and Bi−O Bonds (in Å) in BOC and BOC/PANI

	Bi1−O1	Bi2−O1	Bi2−O2	Bi3−O2	Bi4−O3	Bi4−O4	Bi5−O5	Bi7−O6	Bi7−O8
PANI/BOC	2.394	3.065	2.627	3.258	2.448	2.692	3.236	3.064	3.257
BOC (001)	2.316	2.316	2.316	2.316	2.214	2.214	2.214	2.316	2.316
H···O contact (before)	H1−O1	H1−O3	H1−O4						
	2.800	3.100	2.796						
H···O contact (after)	4.187	2.634	2.676						

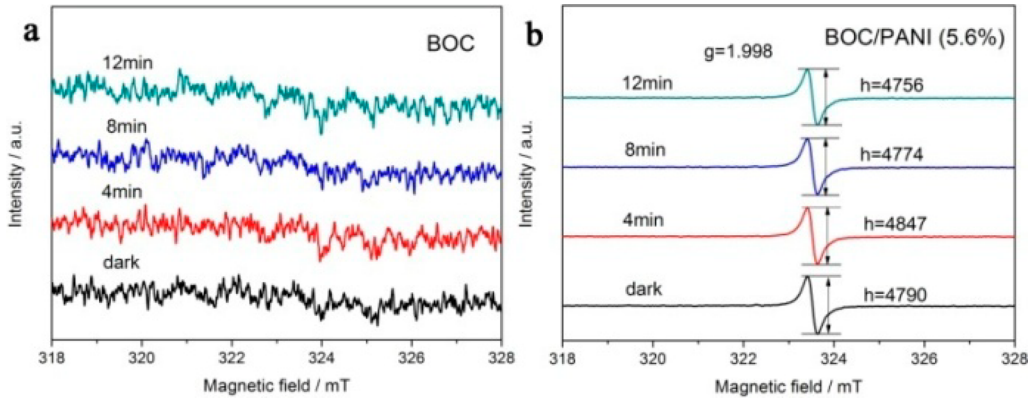

Figure 5. ESR spectra of (a) BOC and (b) BOC/PANI (5.6%) in the darkness and under light irradiation.

distribution of the BOC {001} facets, and chemical bond could be formed at the interface of BOC and PANI.

To shed light on the PANI/BOC (001) interfacial interaction, we further carried out periodic calculations using the first-principle theory. Figure 4 illustrates the computational model and optimized geometries of PANI/BOC (001) interface, and Table 1 lists the lengths of Bi−O and hydrogen bonds at the interface, respectively. For the simulated system, PANI is first assigned nearly vertical to the BOC surface exhibiting H1···O1 distance of 2.8 Å with the principal idea that the H1 atom on NH group of the isolated PANI possesses more positive charge (0.41 e) compared to other H atoms on the benzene ring (about 0.3 e on average), and therefore it tends to form intermolecular hydrogen bond with the O atom on the BOC (001) surface. Whereas after optimization, the H1 atom moves to the top of Bi atom and forms two hydrogen bonds (~2.6 Å) with the adjacent O3 and O4 atoms, as listed in Table1. This gives rise to strong interfacial hydrogen bonding interactions and facilitates charge transfer across the interface. An analysis of Mulliken charge partition scheme indicates a strong 0.24 electron transfer from BOC surface to PANI at the ground electronic state, which consequently results in substantial holes accumulation in BOC (001) slab. Another striking point is that the BOC (001) surface has significant distortions after bridging with PANI via hydrogen bonds as illustrated in Figure 4. The Bi and O atoms are arranged orderly in the BOC (001) surface in Figure 4a, and one O atom bonds with four Bi atoms with the characteristic covalent bond lengths of ~2.3 Å, whereas the atomic arrangement has changed after being modified by PANI, with obvious shifts of the O atoms on the surface due to the interactions with the H atoms on PANI. This strong interfacial interaction leads to the electron redistribution on the BOC (001) surface, and the chemical bonding of Bi−O bonds has changed as a result; in particular, the Bi−O bonds such as Bi3−O2, Bi5−O5, and Bi7−O8 are stretched to more than 3.2 Å, which are almost considered to be broken. This facilities the release of O atoms from the surface of BOC and generates oxygen vacancies. In turn, the BOC surface tends to be more electropositive as observed from XPS results (Figure 3) and benefits in enhancing the photocatalytic activity.[35] To confirm the formation of oxygen vacancy, ESR spectra, which is a common technique to detect defect of materials,[36] were performed on BOC and BOC/PANI (5.6%) samples in the darkness and under visible light irradiation as shown in Figure 5. No ESR signal for BOC sample was observed whether the sample was in the darkness or under light irradiation. Contrarily, there is a remarkable ESR signal from BOC/PANI (5.6%) at g = 1.998, which is typical of oxygen vacancy.[35] In general, the oxygen vacancy is metastable and especially the vacancy located at surface is very easily repaired. Nevertheless, the formed oxygen vacancies in BOC/PANI (5.6%) keep stable even under light irradiation (Figure 5b). Up to the present, the formation of oxygen vacancies is still a challenging task requiring difficult processes such as doping or annealing in a reducing atmosphere.[36] Our current work not only provides a new facile strategy to form oxygen vacancy on the basis of strong interfacial interaction but also demonstrates that the decorated PANI could stabilize oxygen vacancies at the interface of BOC {001} facets and PANI, which is of significance for photocatalytic applications.

3.4. Band Structure and Photogenerated Carrier Behaviors. These strong interfacial interactions between BOC {001} facets and PANI could have a significant influence on their band structures. UV−vis absorption spectra (Supporting Information, Figure S12) reveal that the loading of PANI enhances the absorption of BOC in the visible light range due to the high absorption coefficient of PANI. However, despite the strong interaction and the formation of oxygen vacancy, the band gap of BOC/PANI (5.6%) has no obvious change, which is determined to be 3.32 eV, slightly smaller than that of BOC (3.39 eV). In addition, the valence band (VB) of BOC and BOC/PANI (5.6%) is studied by XPS valence spectra as shown in Figure 3d. The VB maximum of BOC/PANI (5.6%) is 2.37 eV, which is 0.38 eV higher than that of BOC (1.99 eV). Combined with the optical absorption spectra (Figure S12), the conduction band (CB) minimum of BOC/PANI (5.6%) and

DOI: 10.1021/am507089x
ACS Appl. Mater. Interfaces 2015, 7, 730−737

BOC is determined to be −0.95 and −1.40 eV, respectively. Therefore, the interfacial interactions between PANI and BOC resulted in a 0.38 eV down-shifting of VB, indicting a stronger oxidative power of photogenerated holes in the composites.[37,38]

In addition to the optical absorption, charge separation and migration also play a very important role on the photocatalytic reaction process. Hence, electrochemical impedance spectroscopy (EIS) was performed to investigate the photogenerated charge carrier behaviors, as shown in Figure 6. In general, the

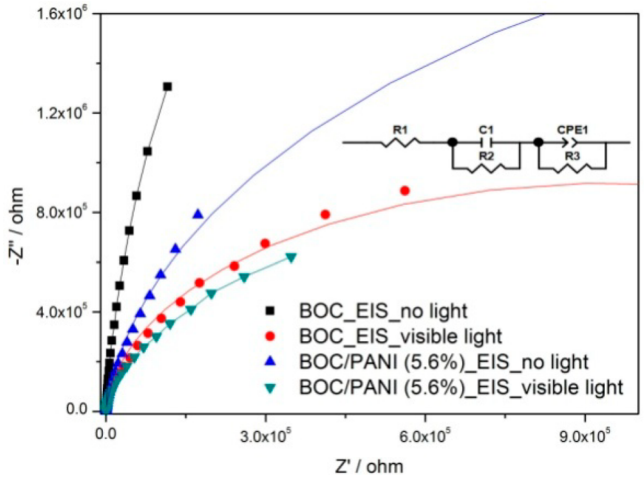

Figure 6. EIS spectra of BOC and BOC/PANI (5.6%) in the darkness and under light irradiation. (inset) Equivalent circuit constructed from BOC and BOC/PANI (5.6%) electrodes.

arc radius on the EIS Nynquist plot reveals reaction rate occurring at the surface of the electrodes.[39] The diameter of the arc radius of both BOC and BOC/PANI (5.6%) is decreased under light irradiation, confirming the generation of photoexcited carriers. Moreover, the radius of the arc of BOC/PANI (5.6%) is smaller than that of BOC no matter whether the sample is in the darkness or under light irradiation. These results indicate an effective separation of photogenerated carriers and fast interfacial charge transfer to the electron acceptor or donor over BOC/PANI (5.6%),[40] agreeing well with the photocurrent measurements (inset, Figure 1b). In addition, inset of Figure 6 shows the equivalent circuit model fitted by the measured data. Here, R1 and R2 represent the resistance of the solution and counter electrode. They keep almost unchanged regardless of loading PANI or under light irradiation (cf. Supporting Information, Table S1). Notably, the resistances of work electrode (R3) decrease 1 order of magnitude after coupling with PANI (Table S1). Therefore, PANI could also improve the conductivity of BOC, which favors the kinetic charge transfer.[41] The lower electron−hole recombination degree over BOC/PANI (5.6%) is reflected from the photoluminescence (PL) spectra (Supporting Information, Figure S13). After the introduction of PANI, the emission intensity of BOC was obviously decreased, suggesting that the radiative recombination of electron−hole pairs on BOC/PANI (5.6%) is suppressed. Furthermore, nanosecond time-resolved emission of BOC/PANI (5.6%) shows faster decay than that of BOC (Figure 7), which is similar to a recent report on BOC/graphene[42] and TiO_2/graphene composites.[43] Using triexponential fitting process, average lifetime of emission decay for BOC and BOC/PANI (5.6%) is calculated to be 5.5 and 3.5 ns, respectively. This decrease of lifetime demonstrates

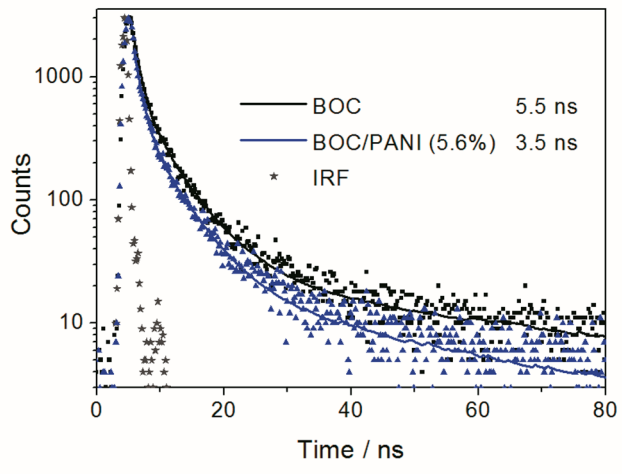

Figure 7. Nanosecond time-resolved emission decay of BOC and BOC/PANI (5.6%). ■ and ▲ represent the original data for BOC and BOC/PANI (5.6%), respectively, and the solid lines are the corresponding fitting results. ★ are the instruments response (IRF). A triexponential fitting process is used to obtain the results.

that some new nonradiative process for charge carriers indeed occurs in BOC after the introduction of PANI. Hence, on the basis of density functional theory (DFT) calculation and ESR results, this new process could be attributed to the combination of excited electrons with the oxygen vacancies, which are generated at the interface of BOC and PANI.

On the basis of the above results, the photoreaction process of BOC and BOC/PANI is proposed as follows. According to the absorption spectra (Figure S12), BOC cannot be excited by light with $\lambda > 420$ nm. Hence, the observed photodegradation of RhB over BOC under visible light is due to the indirect RhB photosensitization.[44] The calculated CB minimum of BOC is −0.76 V versus NHE (Figure 8a), which is more negative than the standard redox potential of O_2/O_2^- (−0.28 V vs NHE), while the redox potentials of RhB and RhB* are 0.95 and −1.42 V versus NHE,[44] respectively. Therefore, under visible light irradiation, the RhB adsorbed on the surface of BOC was excited to generate electrons, which were injected from the excited RhB to the CB of BOC. Then, the electrons were further scavenged by molecular oxygen to yield $O_2^{\bullet-}$ radicals, which finally oxidized RhB molecules (Figure 8a). After coupling with PANI, BOC/PANI can absorb the visible light (Figure S12) due to the excitation of PANI. The π^*- and π-orbital edge potentials are located at −2.14 and 0.62 V versus NHE, respectively.[21] Under visible light irradiation, both RhB and PANI can be excited (Figure 8b). The formed oxygen vacancies at the interfaces could be the center to capture photogenerated electrons during photoreaction process. Consequently, the accumulated electrons on CB of BOC preferably transfer to oxygen vacancy states, which can improve the charge transfer and separation efficiency confirmed by EIS, PL, and time-resolved fluorescence spectra (cf. Figures 6 and 7). The main active species is $O_2^{\bullet-}$ radicals, which have been demonstrated by the comparison experiments under N_2-purged condition.[45] The photodegradation efficiency over both BOC and BOC/PANI (5.6%) decreased sharply with N_2 bubbling into the solution (Supporting Information, Figure S14). BOC exhibited almost no photocatalytic activities in the presence of N_2 bubbling, whereas BOC/PANI (5.6%) showed a reasonable activity. These results indicated after coupling with PANI, the

DOI: 10.1021/am507089x
ACS Appl. Mater. Interfaces 2015, 7, 730−737

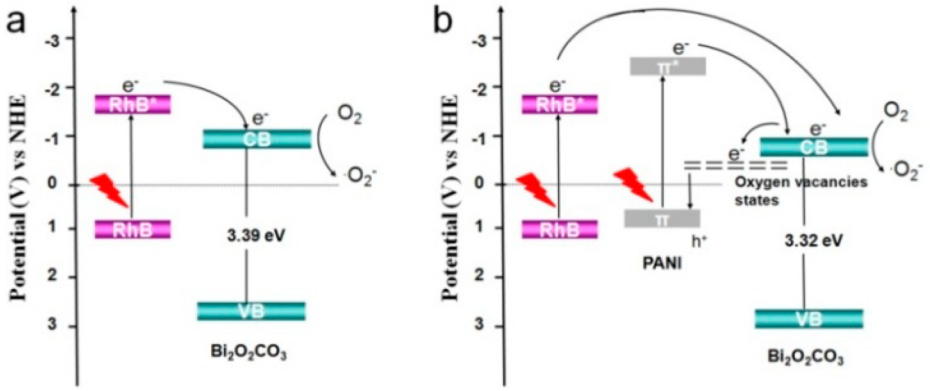

Figure 8. Schematic diagram of charge separation and photocatalytic process over BOC and BOC/PANI under visible light irradiation.

active species is not only $O_2^{\bullet-}$ radicals but also contains hole or $OH^{\bullet-}$, which is due to the activation of PANI and defects.

4. CONCLUSION

In summary, PANI/BOC nanosheets were prepared by a facile chemical method. The high oxygen density and 2D morphology of BOC {001} facets promote intimate and large-area contact between PANI and $Bi_2O_2CO_3$. The strong interaction between PANI and BOC {001} facets not only results in a 0.38 eV downshift of the VB maximum but also promotes in situ oxygen vacancy formation at the interface confirmed by both DFT calculation and ESR analysis. The PANI layer on the BOC can effectively stabilize the formed oxygen vacancies at the interface and increase the conductivity of BOC by 1 order of magnitude, which favors the kinetic charge transfer as well as effective charge separation. Therefore, the resulting BOC/PANI (5.6%) composite exhibited a 4.5 times higher activity toward photodegradation of RhB and a 6 times higher photocurrent density than that of pristine BOC under visible light irradiation. These findings could shed light on the deep understanding of the interactions between PANI and crystal facets of semiconductors to develop highly efficient photocatalysts.

■ ASSOCIATED CONTENT

Supporting Information

Schematic crystal structure of BOC, the adsorption of RhB over BOC and BOC/PANI samples in the dark, the comparison of reaction rate constants, which were normalized to the specific surface area, the variation of NO concentration with irradiation time over BOC and BOC/PANI (5.6%) under visible light irradiation, cycling experiments on the photocatalytic degradation of RhB, the comparsion photodegradation of RhB over fresh sample and sample after two months, XRD patterns, FT-IR, HRTEM, UV−vis diffuse reflectance spectra, PL spectra, and photodegradation of RhB under conventional conduction and with N_2 bubbling into the solution. This material is available free of charge via the Internet at http://pubs.acs.org.

■ AUTHOR INFORMATION

Corresponding Author

*Phone: + 86 28 83037411. Fax: +86 28 83037406. E-mail: yzhou@swpu.edu.cn.

Notes

The authors declare no competing financial interest.

■ ACKNOWLEDGMENTS

We acknowledge the National Natural Science Foundation of China (51102245, U1232119), Sichuan Youth Science and Technology Foundation (2013JQ0034, 2014JQ0017), the Innovative Research Team of Sichuan Provincial Education Department and SWPU (2012XJZT002), and Scientific Research Starting Project of SWPU (2014QHZ020, 2014QHZ021) for financial support. We thank Prof. X. Gong at Nanjing University of Science and Technology for DFT calculation support.

■ REFERENCES

(1) Kudo, A.; Miseki, Y. Heterogeneous Photocatalyst Materials for Water Splitting. *Chem. Soc. Rev.* **2009**, *38*, 253−278.
(2) Chen, X. B.; Shen, S. H.; Guo, L. J.; Mao, S. S. Semiconductor-Based Photocatalytic Hydrogen Generation. *Chem. Rev.* **2010**, *110*, 6503−6570.
(3) Jiang, J.; Zhao, K.; Xiao, X. Y.; Zhang, L. Z. Synthesis and Facet-Dependent Photoreactivity of BiOCl Single-Crystalline Nanosheets. *J. Am. Chem. Soc.* **2012**, *134*, 4473−4476.
(4) Sun, Y. F.; Cheng, H.; Gao, S.; Sun, Z. H.; Liu, Q. H.; Liu, Q.; Lei, F. C.; Yao, T.; He, J. F.; Wei, S. Q.; Xie, Y. Freestanding Tin Disulfide Single-Layers Realizing Efficient Visible-Light Water Splitting. *Angew. Chem., Int. Ed.* **2012**, *51*, 8727−8731.
(5) Zheng, Y.; Duan, F.; Chen, M. Q.; Xie, Y. Synthetic $Bi_2O_2CO_3$ Nanostructures: Novel Photocatalyst with Controlled Special Surface Exposed. *J. Mol. Catal. A* **2010**, *317*, 34−40.
(6) Liu, Y. Y.; Wang, Z. Y.; Huang, B. B.; Yang, K. S.; Zhang, X. Y.; Qin, X. Y. Preparation, Electronic Structure, and Photocatalytic Properties of $Bi_2O_2CO_3$ Nanosheet. *Appl. Surf. Sci.* **2010**, *257*, 172−175.
(7) Chen, L.; Huang, R.; Yin, S.-F.; Luo, S.-L.; Au, C.-T. Flower-Like $Bi_2O_2CO_3$: Facile Synthesis and Their Photocatalytic Application in Treatment of Dye-Containing Wastewater. *Chem. Eng. J.* **2012**, *193*−*194*, 123−130.
(8) Dong, F.; Lee, S. C.; Wu, Z. B.; Huang, Y.; Fu, M.; Ho, W.-K.; Zou, S. C.; Wang, B. Rose-Like Monodisperse Bismuth Subcarbonate Hierarchical Hollow Microspheres: One-pot Template-Free Fabrication and Excellent Visible Light Photocatalytic Activity and Photochemical Stability for NO Removal in Indoor Air. *J. Hazard. Mater.* **2011**, *195*, 346−354.
(9) Zhou, Y.; Wang, H. Y.; Sheng, M.; Zhang, Q.; Zhao, Z. Y.; Lin, Y. H.; Liu, H. F.; Patzke, G. R. Environmentally Friendly Room Temperature Synthesis and Humidity Sensing Applications of Nanostructured $Bi_2O_2CO_3$. *Sens. Actuators, B* **2013**, *188*, 1312−1318.
(10) Zhao, T. Y.; Zai, J. T.; Xu, M.; Zou, Q.; Su, Y. Z.; Wang, K. X.; Qian, X. F. Hierarchical $Bi_2O_2CO_3$ Microspheres with Improved Visible-Light-Driven Photocatalytic Activity. *CrystEngComm* **2011**, *13*, 4010−4017.

DOI: 10.1021/am507089x
ACS Appl. Mater. Interfaces 2015, 7, 730−737

(11) Cao, X. F.; Zhang, L.; Chen, X. T.; Xue, Z. L. Persimmon-Like $(BiO)_2CO_3$ Microstructures: Hydrothermal Preparation, Photocatalytic Properties and Their Conversion into Bi_2S_3. *CrystEngComm* **2011**, *13*, 1939−1945.
(12) Xiong, M.; Chen, L.; Yuan, Q.; He, J.; Luo, S. L.; Au, C. K.; Yin, S. F. Facile Fabrication and Enhanced Photosensitized Degradation Performance of the g-C_3N_4-$Bi_2O_2CO_3$ Composite. *Dalton Trans.* **2014**, *43*, 8331−8337.
(13) Liang, N.; Wang, M.; Jin, L.; Huang, S. S.; Chen, W. L.; Xu, M.; He, Q. Q.; Zai, J. T.; Fang, N. H.; Qian, X. F. Highly Efficient Ag_2O/$Bi_2O_2CO_3$ p-n Heterojunction Photocatalysts with Improved Visible-Light Responsive Activity. *ACS Appl. Mater. Interfaces* **2014**, *6*, 11698−11705.
(14) Xu, Y. S.; Zhang, Z. J.; Zhang, W. D. Inlay of $Bi_2O_2CO_3$ Nanoparticles onto Bi_2WO_6 Nanosheets to Build Heterostructured Photocatalysts. *Dalton Trans.* **2014**, *43*, 3660−3668.
(15) Xu, Y. S.; Zhang, W. D. Anion Exchange Strategy for Construction of Sesame-biscuit-like $Bi_2O_2CO_3$/Bi_2MoO_6 Nanocomposites with Enhanced Photocatalytic Activity. *Appl. Catal., B* **2013**, *140*, 306−316.
(16) Cai, G. Y.; Xu, L. L.; Wei, B.; Chen, J. X.; Gao, H.; Sun, W. J. Facile Synthesis of β-Bi_2O_3/$Bi_2O_2CO_3$ Nanocomposite with High Visible-light Photocatalytic Activity. *Mater. Lett.* **2014**, *120*, 1−4.
(17) Liang, C.; Yin, S. F.; Luo, S. L.; Huang, R.; Zhang, Q.; Hong, T.; Au, P. C. T. $Bi_2O_2CO_3$/BiOI Photocatalysts with Heterojunctions Highly Efficient for Visible-Light Treatment of Dye-Containing Wastewater. *Ind. Eng. Chem. Res.* **2012**, *51*, 6760−6768.
(18) Zhang, H.; Zong, R. L.; Zhao, J. C.; Zhu, Y. F. Dramatic Visible Photocatalytic Degradation Performances Due to Synergetic Effect of TiO_2 with PANI. *Environ. Sci. Technol.* **2008**, *42*, 3803−3807.
(19) Radoičić, M.; Šaponjić, Z.; Janković, I. A.; Ćirić-Marjanović, G.; Ahrenkiel, S. P.; Čomor, M. I. Improvements to the Photocatalytic Efficiency of Polyaniline Modified TiO_2 Nanoparticles. *Appl. Catal., B* **2013**, *136*−*137*, 133−139.
(20) Pei, Z. X.; Ding, L. Y.; Lu, M. L.; Fan, Z. H.; Weng, S. X.; Hu, J.; Liu, P. Synergistic Effect in Polyaniline-Hybrid Defective ZnO with Enhanced Photocatalytic Activity and Stability. *J. Phys. Chem. C* **2014**, *118*, 9570−9577.
(21) Ge, L.; Han, C. C.; Liu, J. In situ Synthesis and Enhanced Visible Light Photocatalytic Activities of Novel PANI−g-C_3N_4 Composite Photocatalysts. *J. Mater. Chem.* **2012**, *22*, 11843−11850.
(22) Wang, Q. Z.; Hui, J.; Li, J. J.; Cai, Y. X.; Yin, S. Q.; Wang, F. P.; Su, B. T. Photodegradation of Methyl Orange with PANI-Modified BiOCl Photocatalyst under Visible Light Irradiation. *Appl. Surf. Sci.* **2013**, *283*, 577−583.
(23) Hou, J. G.; Cao, R.; Jiao, S. Q.; Zhu, H. M.; Kumar, R. V. PANI/$Bi_{12}TiO_{20}$ Complex Architectures: Controllable Synthesis and Enhanced Visible-Light Photocatalytic Activities. *Appl. Catal., B* **2011**, *104*, 399−406.
(24) Wang, W. Z.; Xu, J. H.; Zhang, L.; Sun, S. M. Bi_2WO_6/PANI: An Efficient Visible-Light-Induced Photocatalytic Composite. *Catal. Today* **2014**, *224*, 147−153.
(25) Yang, H. G.; Sun, C. H.; Qiao, S. Z.; Zou, J.; Liu, G.; Smith, S. C.; Cheng, H. M.; Lu, G. Q. Anatase TiO_2 Single Crystals with a Large Percentage of Reactive Facets. *Nature* **2008**, *453*, 638−641 b).
(26) Pan, J.; Liu, G.; Lu, G. Q.; Cheng, H. M. On the True Photoreactivity Order of {001}, {010}, and {101} Facets of Anatase TiO_2 Crystals. *Angew. Chem., Int. Ed.* **2011**, *50*, 2133−2137.
(27) Xie, X. W.; Li, Y.; Liu, Z.-Q.; Haruta, M.; Shen, W. J. Low-Temperature Oxidation of CO Catalysed by Co_3O_4 Nanorods. *Nature* **2009**, *458*, 746−749.
(28) Clark, S. J.; Segall, M. D.; Pickard, C. J.; Hasnip, P. J.; Probert, M. I. J.; Refson, K.; Payne, M. C. First Principles Methods Using CASTEP. *Z. Kristallogr.* **2005**, *220*, 567−570.
(29) Zhang, Q.; Zhou, Y.; Wang, F.; Dong, F.; Li, W.; Li, H. M.; Patzke, G. R. From Semiconductors to Semimetals: Bismuth as Photocatalyst for NO Oxidation in Air. *J. Mater. Chem. A* **2014**, *2*, 11065−11072.
(30) Guan, M. L.; Xiao, C.; Zhang, J.; Fan, S. J.; An, R.; Cheng, Q. M.; Xie, J. F.; Zhou, M.; Ye, B. J.; Xie, Y. Vacancy Associates Promoting Solar-Driven Photocatalytic Activity of Ultrathin Bismuth Oxychloride Nanosheets. *J. Am. Chem. Soc.* **2013**, *135*, 10411−10417.
(31) Zhou, Y.; Zhang, X. J.; Zhao, Z. Y.; Zhang, Q.; Wang, F.; Lin, Y. H. Effects of pH on the Visible-Light Induced Photocatalytic and Photoelectrochemical Performances of Bi_2WO_6. *Superlattices Microstruct.* **2014**, *72*, 238−244.
(32) Dong, F.; Zheng, A. M.; Sun, Y. J.; Fu, M.; Jiang, B. Q.; Ho, W.-K.; Lee, S. C.; Wu, Z. B. One-Pot Template-Free Synthesis, Growth Mechanism and Enhanced Photocatalytic Activity of Monodisperse $(BiO)_2CO_3$ Hierarchical Hollow Microspheres Self-Assembled with Single-Crystalline Nanosheets. *CrystEngComm* **2012**, *14*, 3534−3544.
(33) Janáky, C.; Tacconi, N. R. de.; Chanmanee, W.; Rajeshwar, K. Electrodeposited Polyaniline in a Nanoporous WO_3 Matrix: An Organic/Inorganic Hybrid Exhibiting Both p- and n-Type Photoelectrochemical Activity. *J. Phys. Chem. C* **2012**, *116*, 4234−4242.
(34) Madhusudan, P.; Ran, J.; Zhang, J.; Yu, J. G. Novel Urea Assisted Hydrothermal Synthesis of Hierarchical $BiVO_4$/$Bi_2O_2CO_3$ Nanocomposites with Enhanced Visible-Light Photocatalytic Activity. *Appl. Catal., B* **2011**, *110*, 286−295.
(35) Pei, Z. X.; Ding, L. Y.; Hu, J.; Weng, S. X.; Zheng, Z. Y.; Huang, M. L.; Liu, P. Defect and its Dominance in ZnO Films: a New Insight into the Role of Defect Over Photocatalytic Activity. *Appl. Catal., B* **2013**, *142*−*143*, 736−743.
(36) Ye, L. Q.; Deng, K. J.; Xu, F.; Tian, L. H.; Peng, T. Y.; Zan, L. Increasing Visible-Light Absorption for Photocatalysis with Black BiOCl. *Phys. Chem. Chem. Phys.* **2012**, *14*, 82−85.
(37) Shi, R.; Huang, G. L.; Lin, J.; Zhu, Y. F. Photocatalytic Activity Enhancement for Bi_2WO_6 by Fluorine Substitution. *J. Phys. Chem. C* **2009**, *113*, 19633−19638.
(38) Zhou, Y.; Zhang, X. J.; Zhang, Q.; Dong, F.; Wang, F.; Xiong, Z. Role of Graphene on the Band Structure and Interfacial Interaction of Bi_2WO_6/Graphene Composites with Enhanced Photocatalytic Oxidation of NO. *J. Mater. Chem. A* **2014**, *2*, 16623−16631.
(39) Lei, F. C.; Sun, Y. F.; Liu, K. T.; Gao, S.; Liang, L.; Pan, B. C.; Xie, Y. Oxygen Vacancies Confined in Ultrathin Indium Oxide Porous Sheets for Promoted Visible-Light Water Splitting. *J. Am. Chem. Soc.* **2014**, *136*, 6826−6829.
(40) Zhou, Y.; Zhang, Q.; Lin, Y. H.; Antonova, E.; Bensch, W.; Patzke, G. R. One-Step Hydrothermal Synthesis of Hierarchical Ag/Bi_2WO_6 Composites: In Situ Growth Monitoring and Photocatalytic Activity Studies. *Sci. China Chem.* **2013**, *56*, 435−442.
(41) Xu, X. X.; Randorn, C.; Efstathiou, P.; Irvine, J. T. S. A Red Metallic Oxide Photocatalyst. *Nat. Mater.* **2012**, *11*, 595−598.
(42) Zhang, Y. L.; Li, D. Y.; Zhang, Y. G.; Zhou, X. F.; Guo, S. J.; Yang, L. B. Graphene-Wrapped $Bi_2O_2CO_3$ Core-Shell Structures with Enhanced Quantum Efficiency Profit from an Ultrafast Electron Transfer Process. *J. Mater. Chem. A* **2014**, *2*, 8273−8280.
(43) Sun, J.; Zhang, H.; Guo, L. H.; Zhao, L. X. Two-Dimensional Interface Engineering of a Titania-Graphene Nanosheet Composite for Improved Photocatalytic Activity. *ACS Appl. Mater. Interfaces* **2013**, *5*, 13035−13041.
(44) Hu, J. L.; Fan, W. J.; Ye, W. Q.; Huang, C. J.; Qiu, X. Q. Insights into the Photosensitivity Activity of BiOCl under Visible Light Irradiation. *Appl. Catal., B* **2014**, *158*−*159*, 182−189.
(45) Park, Y.; Lee, S. H.; Kang, S. O.; Choi, W. Organic Dye-Sensitized TiO_2 for the Redox Conversion of Water Pollutants under Visible Light. *Chem. Commun.* **2010**, *46*, 2477−2479.

DOI: 10.1021/am507089x
ACS Appl. Mater. Interfaces 2015, 7, 730−737